

Article

Improvement and Impacts of Forest Canopy Parameters on Noah-MP Land Surface Model from UAV-Based Photogrammetry

Ming Chang ^{1,†} , Shengjie Zhu ^{2,†} , Jiachen Cao ¹ , Bingyin Chen ¹ , Qi Zhang ³ , Weihua Chen ¹ , Shiguo Jia ³ , Padmaja Krishnan ⁴  and Xuemei Wang ^{1,*} 

¹ Guangdong-Hongkong-Macau Joint Laboratory of Collaborative Innovation for Environmental Quality, Institute for Environmental and Climate Research, Jinan University, Guangzhou 510443, China; changming@email.jnu.edu.cn (M.C.); jiachenc@stu2018.jnu.edu.cn (J.C.); chenbingyin16@mails.ucas.ac.cn (B.C.); chenwh26@jnu.edu.cn (W.C.)

² Department of Environmental Science, Guangdong Polytechnic of Environmental Protection Engineering, Foshan 528216, China; zhushj@mail3.sysu.edu.cn

³ Guangdong Province Key Laboratory for Climate Change and Natural Disaster Studies, School of Atmospheric Sciences, Sun Yat-sen University, Guangzhou 510275, China; zhangq358@mail2.sysu.edu.cn (Q.Z.); jiashg3@mail.sysu.edu.cn (S.J.)

⁴ Department of Civil & Environmental Engineering, National University of Singapore, Singapore 117576, Singapore; ceekp@nus.edu.sg

* Correspondence: eciwxm@jnu.edu.cn

† These authors contributed equally to this work.

Received: 26 October 2020; Accepted: 14 December 2020; Published: 16 December 2020



Abstract: Taking a typical forest's underlying surface as our research area, in this study, we employed unmanned aerial vehicle (UAV) photogrammetry to explore more accurate canopy parameters including the tree height and canopy radius, which were used to improve the Noah-MP land surface model, which was conducted in the Dinghushan Forest Ecosystem Research Station (CN-Din). While the canopy radius was fitted as a Burr distribution, the canopy height of the CN-Din forest followed a Weibull distribution. Then, the canopy parameter distribution was obtained, and we improved the look-up table values of the Noah-MP land surface model. It was found that the influence on the simulation of the energy fluxes could not be negligible, and the main influence of these canopy parameters was on the latent heat flux, which could decrease up to -11% in the midday while increasing up to 15% in the nighttime. Additionally, this work indicated that the description of the canopy characteristics for the land surface model should be improved to accurately represent the heterogeneity of the underlying surface.

Keywords: forest canopy parameters; UAV-based photogrammetry; land surface modeling

1. Introduction

The land surface process is the lower boundary condition of atmospheric movement, and the different types of underlying surface have multiple weather and climate effects [1]. The development of land surface models provides a way to help us understand the complex processes and interactions between the land surface and the atmosphere across micro to global scales. It can provide a simple and realistic way to show the transfer of energy, mass and momentum through the numerical parameterization of land surface models [2]. It is well known that the differences in underlying surface characteristics are embodied by using different land surface parameters [3]. Generally, the measurement of pollutant deposition and the estimation of ecological impact depend on the accuracy of the

simulation results of land–air exchange flux; thus, the improvement of canopy properties is urgently needed for the modeling of land–atmosphere interaction processes [4].

Additionally, the creation of land surface models and coupled atmosphere and environment models can be improved by refining the land surface inputs and parameters [5]. However, the treatment of vegetation, especially the forest canopy structure, has been set as one large leaf in land surface models for a long time [6]. The vegetation canopy is commonly defined by the canopy top and bottom, crown radius and leaves with prescribed dimensions, orientation density, and radiometric properties [7]. Although some 3D computer simulation models are suitable for studying smaller-scale scenes with fine structures, the demands of extreme computational resources have still made it difficult for them to be applied at a large scale [8]. In this case, the range of typical parameter values in forests remains a large source of uncertainty [4].

The parameterizations about the forest canopy structure of land surface models that are commonly coupled in meteorological or climate simulations are listed in Table 1 [9–15]. Different parameterization schemes divide the canopy into one layer, two layers or multiple layers to calculate the energy decomposition or radiative transfer in the canopy [16–19]. For the calculation of the atmospheric dynamic process, the current land surface models that have been widely used in climate and hydrology researches, such as simple biosphere model (SiB4) and biosphere atmosphere transfer scheme (BATS), are based on the measured empirical wind speed profile in the canopy and provide an empirical solution to calculate the turbulent exchange in the canopy [20,21].

Unmanned aerial vehicles (UAVs) provide an effective platform for quickly and cheaply obtaining the parameters of vegetation canopies [22]. This technique has been expected to become increasingly common in forest studies with the availability of more efficient data processing software [23,24]. The communities have begun using UAVs to map canopy gaps, tree heights and leaf angles, etc. [25–28]. Furthermore, UAV-borne LiDAR systems could allow the accuracy of the parameter measurements to reach the centimeter level, which would noticeably influence the surface wind profile and momentum [23,29,30]. Additionally, UAV photogrammetry can obtain more abundant spectral characteristics of images, which is important for vegetation species identification; therefore, it would potentially improve the accuracy of air quality numerical models and climate models [31]. However, the application of measurement results from these above techniques and the performance of mass and energy exchange simulations between ecosystems and the atmosphere in land surface models still needs further exploration.

In this study, a typical subtropical forest's underlying surface was taken as the research area; we mainly focused on the establishment of the connection between forest canopy parameters including the tree heights and crown radius of this forest by UAV photogrammetry and obtained these accurate canopy parameters for land surface model improvement. With these canopy parameters used to replace the original default value of the model, the difference of the simulated heat flux caused by using these accurately obtained canopy parameters was explored.

Table 1. Forest canopy parameterization in land surface models.

Land Surface Models	Noah	Noah-MP	CLM	RUC	SSiB	PX
Vegetative components	One vegetation type in one gridcell without dynamic vegetation and carbon budget	One vegetation type in one gridcell with dynamic vegetation and carbon budget	Subgrids with up to 10 vegetation types in one gridcell with dynamic vegetation and carbon budget	Multiple vegetation types by using land use fractions in one gridcell without dynamic vegetation and carbon budget	One vegetation type in one gridcell without dynamic vegetation and carbon budget	One vegetation type in one gridcell without dynamic vegetation and carbon budget
Photosynthetic pathway	No	Yes, ¶ = 1	Yes, ¶ = 1	No	No	Yes, § = 1
Phenology	Yes, ¶ = 1	Yes, § = 1	Yes, † = 1	Yes, ¶ = 1	No	Yes, ¶ = 1
Relative leaf nitrogen profile	No	Yes, ¶ = 2	Yes, § = 1	No	No	No
Leaf dimension	No	No	Yes, ¶ = 1	No	Yes, ¶ = 1	No
Leaf area index	Yes, ¶ = 1	Yes, ¶ = 2	Yes, ¶ = 2	Yes, ¶ = 2	Yes, ¶ = 1	Yes, § = 1
Canopy heights	Yes, ¶ = 2	Yes, ¶ = 2	Yes, ¶ = 2	No	Yes, ¶ = 1	No
Length of live crown	No	No	No	No	No	No
Length of dead crown	No	No	No	No	No	No
Crown radius	No	Yes, ¶ = 1	Yes, ¶ = 1	No	No	No
Number of branches	No	Yes, ¶ = 1	No	No	No	No
Branch zenith	No	No	No	No	No	No

¶: Number of parameters; §: Using subroutines; †: Using modules (multiple subroutines).

2. Materials and Methods

2.1. Study Area and Field Data Collection

The study was carried out in the Dinghushan Forest Ecosystem Research Station, which represents the subtropical forest areas in South China (Fluxnet Site Code: CN-Din). This site is located in the Dinghushan biosphere reserve in Zhaoqing, Guangdong province, China (as shown in Figure 1, and also in Chang et al. [32]). The majority of the area is covered by a 100-year-old subtropical evergreen broadleaf and pine–broadleaf mixed forest, mainly consisting of *Castanopsis chinensis*, *Schima superba* and *Pinus massoniana*, etc. [33,34]. The vegetation is fairly homogeneous within a distance of ~ 1 km in the direction of the dominant wind direction (northeast). The gap area accounts for 3~25% of forest area, and the average size is about 80~100 m², which makes it difficult to use a larger UAV to carry LiDAR instruments or other big equipment. UAV images over the study site were collected between August 2019 to September 2019, as part of a comprehensive observation experiment in CN-Din [35].

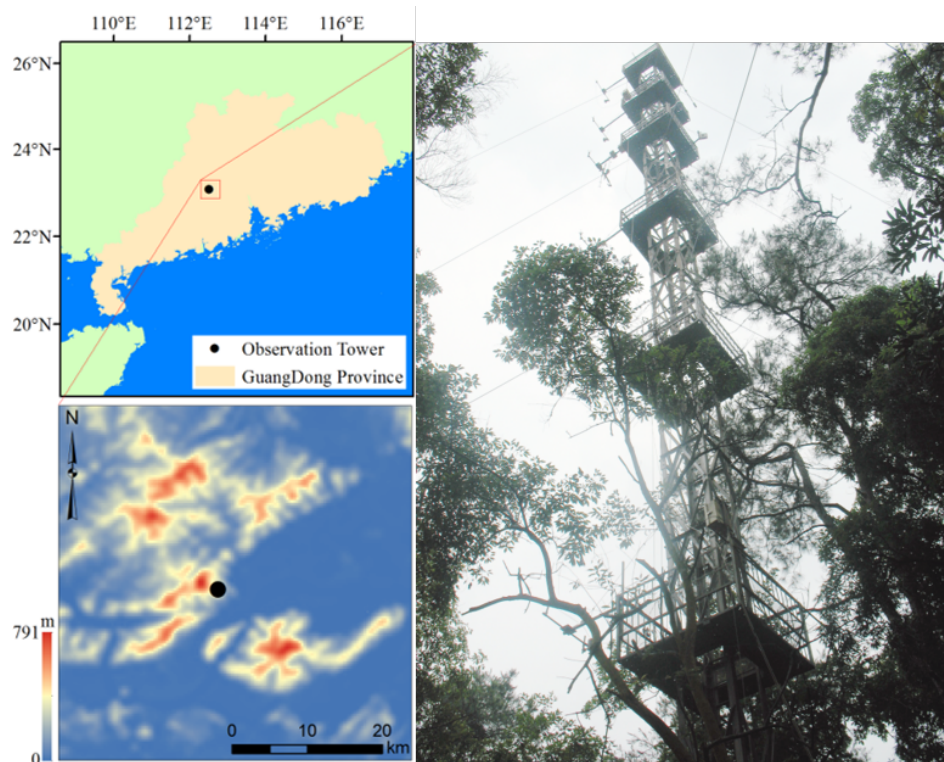


Figure 1. Location and geographic features of Dinghushan Station.

2.2. Workflow from UAV Photogrammetry to Land-Atmospheric Simulation

A workflow was developed to calculate the canopy parameters required to improve the land surface model using UAV photogrammetry (Figure 2). We used the built-in tools and algorithms to process the UAV images from a set of images on the same subject, by means of structure from motion (SfM) techniques [36,37]. Three-dimensional reconstruction terrain-oriented software was employed to create the point clouds and orthomosaics [38]. Additionally, a state-of-the-art land surface model was employed to investigate the effects of UAV-based photogrammetry for the extraction of precise forest canopy parameters as inputs for meteorological or climate models [39].

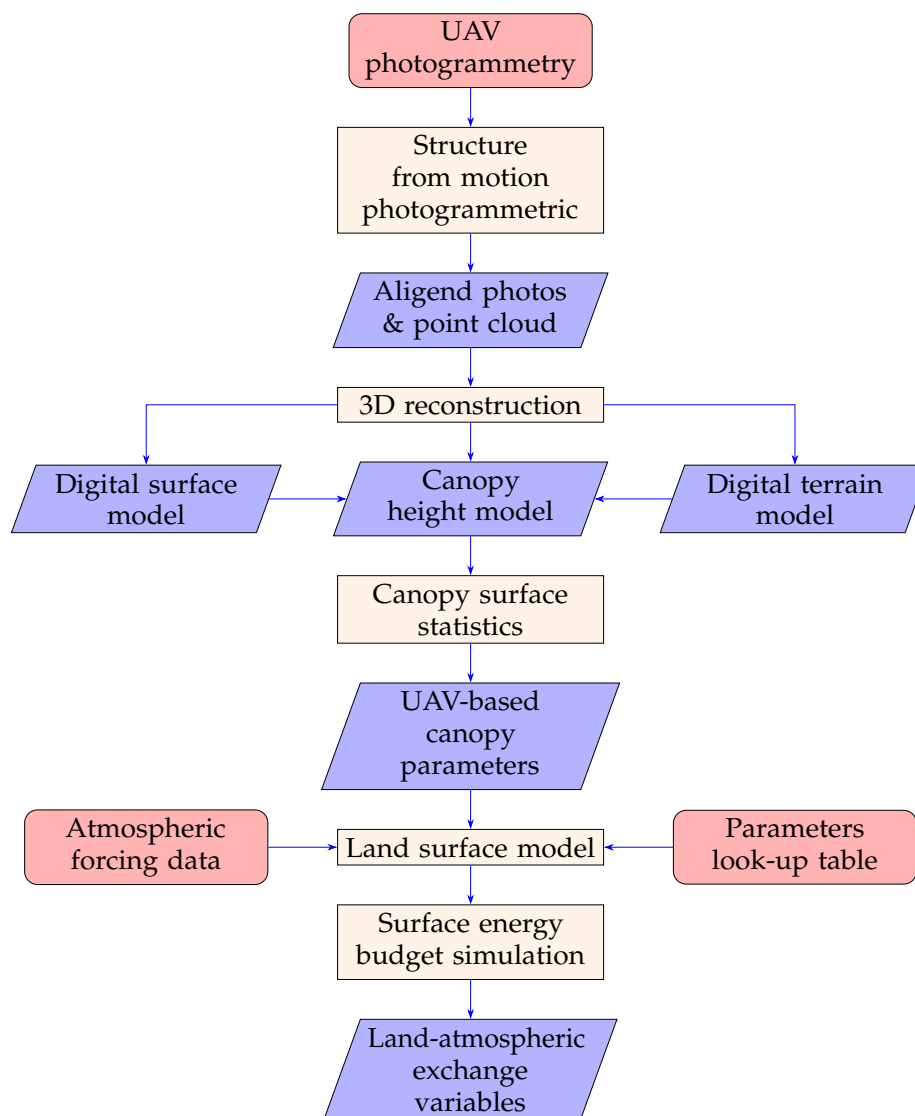


Figure 2. Main workflow to estimate the effects of land–air energy budgets by refined canopy parameters from high-resolution unmanned aerial vehicle (UAV) photogrammetry.

2.3. Airborne Equipment and Processing Software Setup

A DJI Phantom 3 Professional UAV equipped with a classic FC300X_3.6_4000x3000 (RGB) camera was used for image acquisition. The equipment is mature, stable, low cost, easy to carry and moderately difficult to operate. The comparison of the equipment is shown in Table 2. It can be seen that the camera is a non-professional measuring camera—the lens is not strictly calibrated and there is no set control point for calibration—and so the digital image captured has an optical distortion error. In addition, compared with LiDAR, the ability of visible light cameras to acquire forest interlayer structures is insufficient [23].

Furthermore, the UAV flies horizontally and the camera lens tilts downward at about 45 degrees. The pilot manually operated the UAV, creating circular flight paths over the target area. The average flight altitude for this study was set at 100 m with a horizontal velocity of about 3 m/s (as shown in Figure 3). This resulted in photographs with a ground sample distance (GSD) of 7.2 cm on average. The flight line was planned for the images to have an 85% overlap in flight direction and 60% side overlap. The Pix4D software was then used to create a dense point cloud with a mean point density of 42.6 points/m for the 100 m high flights [38]. There were 55,520 (median) keypoints per image in total; 67 out of 67 images were calibrated (100%) and all images enabled a dataset quality check. The relative

difference between the initial and final focal length was 3.19% for camera optimization, and the median of the number of matches per calibrated image was 19,330.2. The root mean square error (RMSE) of the absolute geolocation variance in each direction was (X 1.40%, Y 2.34%, Z 0.53%). Point cloud data were divided into six categories: unclassified, ground, road surface, high vegetation, building and other human-made objects. The ground and high vegetation data were required for this study out of the six categories of point cloud data. In addition to the point cloud data, a digital orthophoto model (DOM) and digital surface model (DSM) were also output. Then, a canopy height model was derived by subtracting the DOM from the DSM using the Green Valley International LiDAR360 software [40]. Finally, the parameters of the canopy, including the tree height and tree radius, were built from the point cloud and the canopy height model [41].

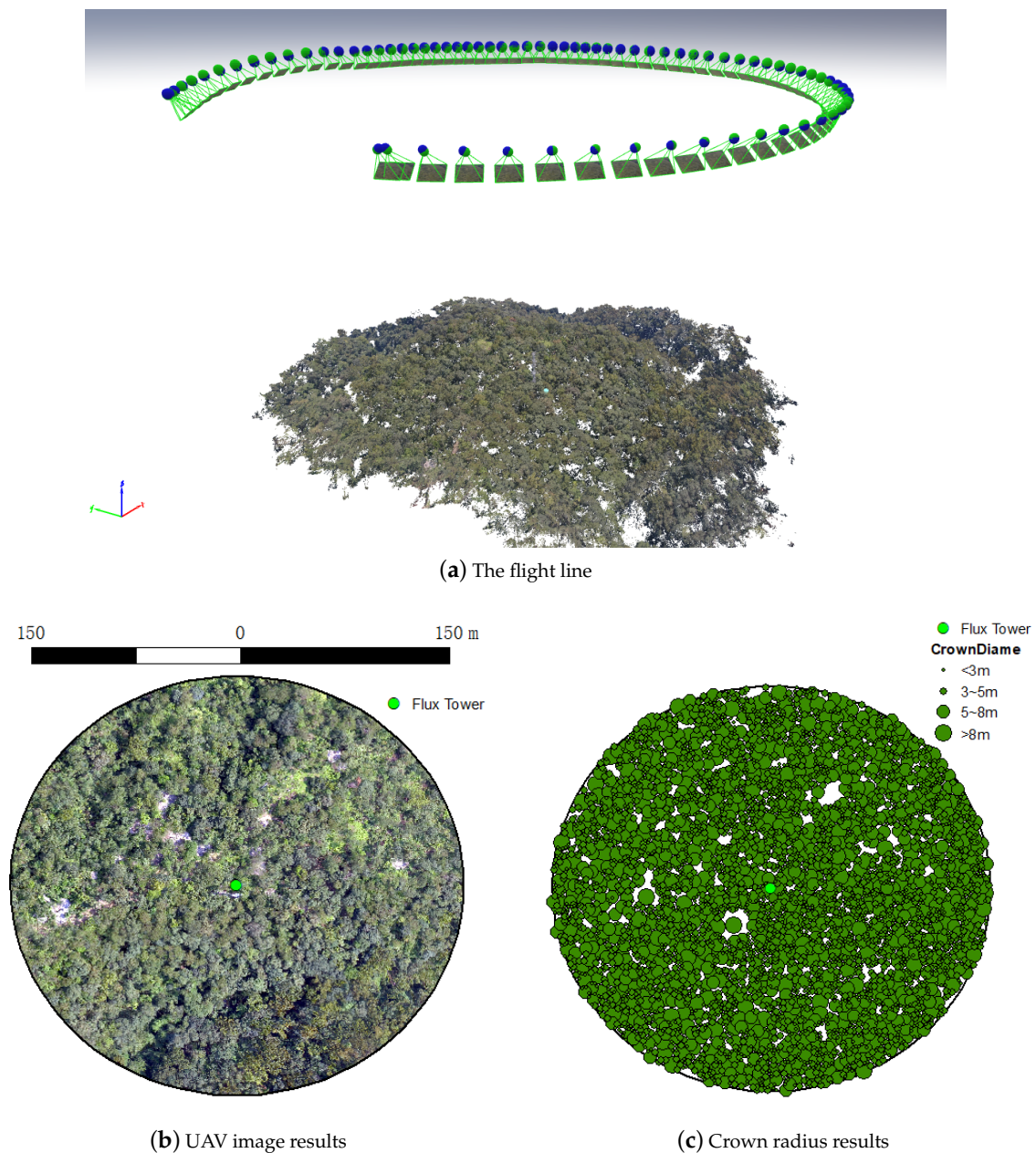


Figure 3. The flight line and UAV image acquisition results.

Table 2. Comparison of common measurement schemes for consumer and professional UAVs.

Platform & Scheme	DJI Phantom 3 Professional	DJI M600 Equipped with Five-Lens Tilt Camera	DJI M600 Equipped with Lidar
Full weight of equipments	~4 kg	~30 kg	~30 kg
Packaging & dimensions of transport	390 × 360 × 210 mm	525 × 480 × 640 mm	525 × 480 × 640 mm
Procurement cost	~CNY10,000	~CNY110,000	~CNY210,000
Operator	1~2 person	2~3 person	2~3 person
Main advantage	Low cost, easy to carry and moderate operation difficulty	Higher measurement and can obtain more abundant spectral characteristics of images	Highest measurement accuracy and strong penetration ability

2.4. Land Surface Model Setup

In this work, we chose the Noah-MP land surface model to estimate the effects of the updated parameters. This model—as a state-of-the-art model—consists of 12 biophysical and hydrological processes that control heat fluxes between the surface and the atmosphere. Additionally, these processes also include dynamic vegetation, stomatal conductance, surface exchange coefficients for heat and water vapor, radiation interactions with the vegetation canopy and the soil, hydrological processes within the canopy and the soil, a multi-layer snowpack and a frozen ground and aquifer model for groundwater dynamics [13].

On the other hand, due to the lack of observed surface heat flux data during the UAV flight, we evaluated the simulation impact of UAV-based parameters by using the validated benchmark observation dataset, which has been analyzed in our previous study; i.e., Zhang et al. [42]. Table 3 shows the setup of option combinations, which were verified and chosen by an ensemble simulation test [32]. The average monthly diurnal latent heat flux (LH) and sensible heat flux (SH) obtained from observations and simulated from the option combinations in the previous study are shown in Figure 4. It is worth noting that this setup of Noah-MP was able to closely simulate SH in spring, autumn and winter months, while overestimating SH during June to September and underestimating LH in the midday during these months.

Table 3. The setup option of the Noah-MP land surface model.

Physical Processes	Options	Reference
Options for dynamic vegetation	Dynamic vegetation model	Dickinson et al. [43]
Options for canopy stomatal resistance	Ball-Berry scheme	Ball et al. [44]
Options for soil moisture factor for stomatal resistance	Noah type (based on soil moisture)	Chen et al. [45]
Options for runoff and groundwater	Simple groundwater model (SIMGM)	Niu et al. [46]
Options for surface layer drag coefficient	Original Noah (Chen97)	Chen et al. [47]
Options for radiation transfer	Modified two-stream, $gap = f(3Dstructure, solarangle)$	Niu and Yang [48]
Options for frozen soil permeability	Linear effects, more permeable (NY06)	Niu and Yang [49]
Options for supercooled liquid water	No iteration (NY06)	Niu and Yang [49]
Options for ground snow surface albedo	Canadian land surface scheme (CLASS)	Verseghy [50]
Options for partitioning precipitation into rainfall & snowfall	Jordan scheme	Jordan [51]
Options for lower boundary condition of soil temperature	TBOT at ZBOT (8m) read from a file (original Noah)	Barlage et al. [52]
Options for snow and soil temperature time scheme	Semi-implicit	Niu et al. [13]

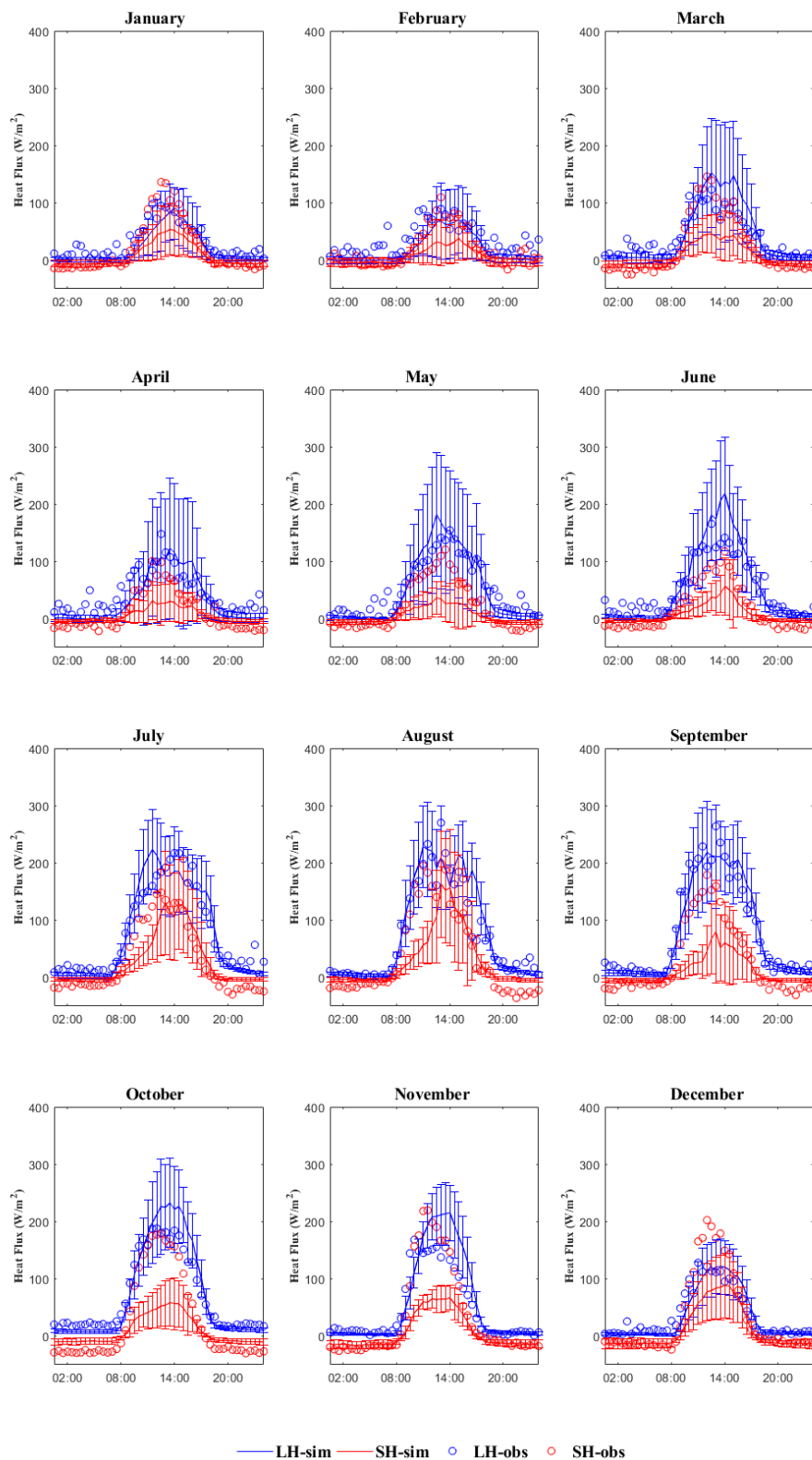


Figure 4. The monthly average diurnal latent heat flux (LH) and sensible heat flux (SH) results from observations and simulated with the original parameters.

3. Results

3.1. Comparison of UAV-Based and Model-Original Canopy Parameters

The description of the forest canopy characteristics in the land surface model was still set by a landcover map with an attribute look-up table, although the observation techniques significantly improved the ability to determine canopy-structure variables over large areas. As shown in Figure 5, the forests were divided into five classifications in the Noah-MP model, which included deciduous broadleaf forest, deciduous needleleaf forest, evergreen broadleaf forest, evergreen needleleaf forest and mixed forest.

The main differences among these forest types were the tree canopy top height, canopy bottom height and the crown radius. The quantities of tree heights and crown radii observed by the UAV method are also shown in Figure 5. This shows that the distribution of the Dinghushan forest appeared to present two stages, which could indicate the characteristics of a successional subtropical forest. It should be noted that the measurement accuracy in this study is not as good as that using professional visible light measurement equipment, and the acquisition ability of the forest interlayer structure is not as good as that of LiDAR. Compared with LiDAR techniques, the ability of visible light photographs to acquire the forest interlayer structure was still insufficient [23]. However, compared with the current parameter look-up table in the Noah-MP land surface model, the result of photogrammetry significantly increased the accuracy.

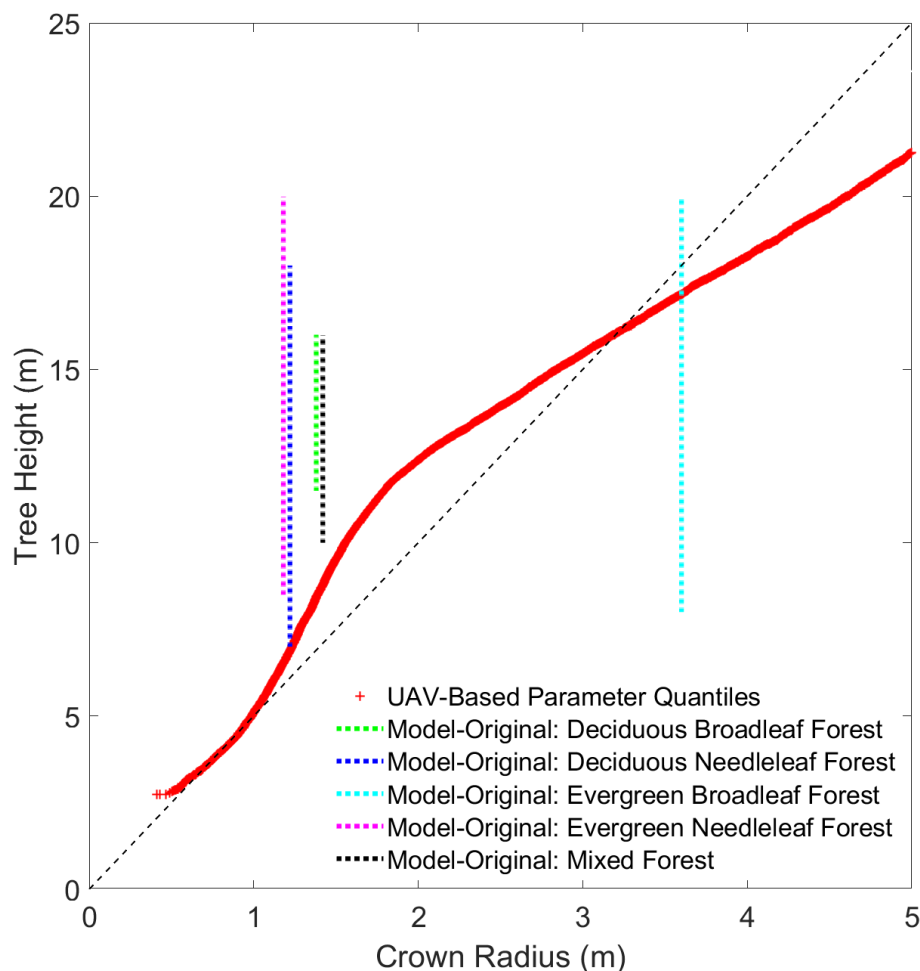
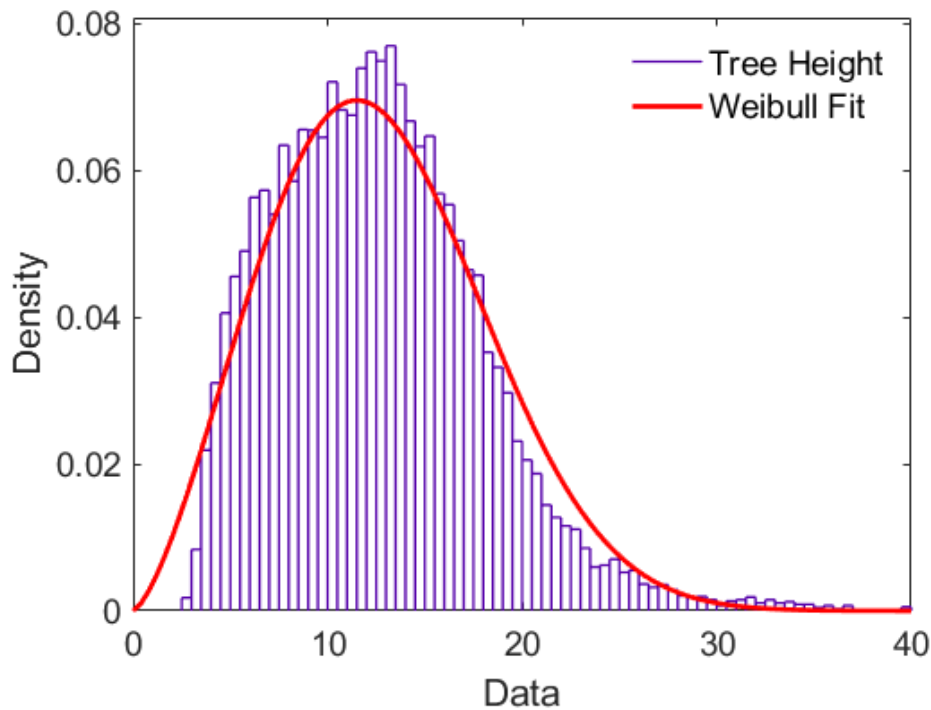
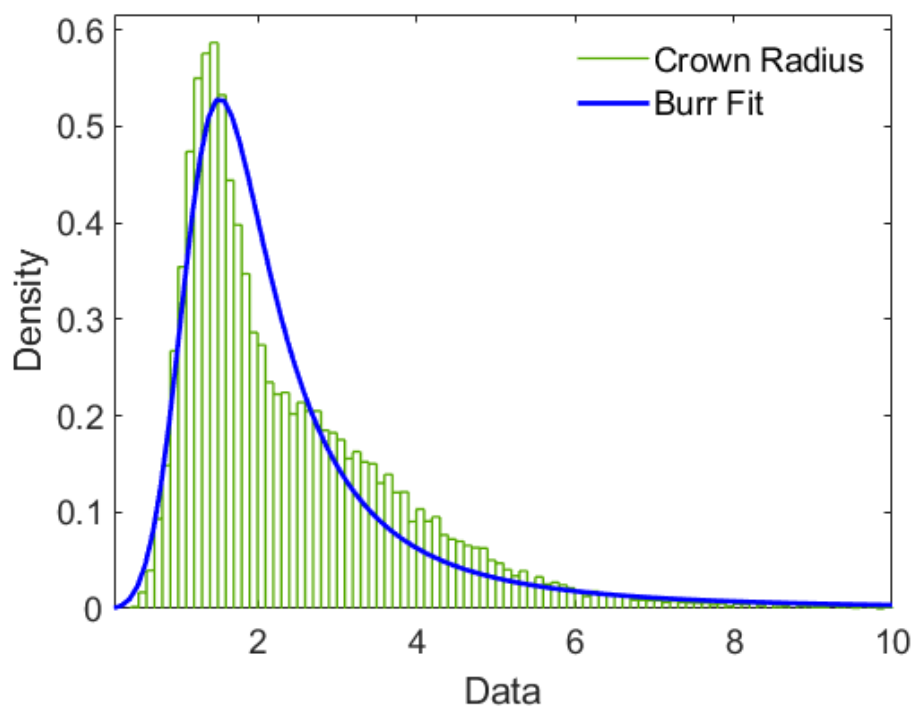


Figure 5. The distribution of UAV-based canopy parameters and the model-original look-up table values.

Additionally, the histograms of these two parameters (tree heights and crown radius) are shown in Figure 6, and the corresponding distributions were fitted as Weibull or Burr distributions, while the functions and coefficients are listed in Table 4. It can be seen from Figure 6 that the medians (standard deviations) of the tree height and crown radius were 12.2 ± 5.4 m and 1.9 ± 1.5 m, respectively. These features were replaced into the attribute look-up table and then used for the Noah-MP model, which is further discussed in Sections 3.2 and 4.1.



(a) Tree height fitting



(b) Crown radius fitting

Figure 6. Histogram and distribution fits of UAV-based canopy parameters.

Table 4. Fitted coefficients for the distribution of UAV-based canopy parameters.

Canopy Parameter	Dist Type	Functions	Coefficients
Tree height	Weibull	$f(x a, b) = \frac{b}{a} \left(\frac{x}{a}\right)^{b-1} e^{-(x/a)^b}$	$a = 14.26, b = 2.44$
Crown radius	Burr	$f(x \alpha, c, k) = 1 - \frac{1}{\left(1 + \left(\frac{x}{\alpha}\right)^c\right)^k}$	$\alpha = 1.46, c = 4.73, k = 0.44$

3.2. Performance of the Surface Energy Budget Simulation

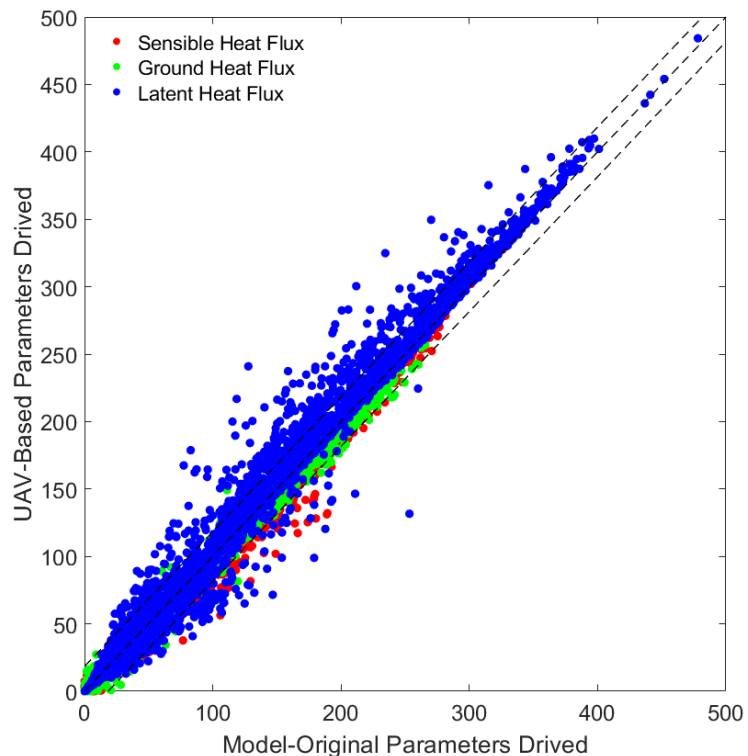
The effect of replacing the model's original canopy parameters with the results obtained from the UAV on the surface energy components is shown in Figure 7. It can be seen that, after replacing parameters, most of the SH and ground heat flux (G) values were not significantly changed, and only a few points exceeded the 10% standard derivation threshold line (black dash line in Figure 7a), which corresponded to a significant change. After using more accurate canopy parameters, the SH changed at a range from -5.5 to 1.7 W/m^2 with a slightly decreased mean (-0.2 W/m^2), and the G was basically stable at the mean value of $2.7 \times 10^{-5} \text{ W/m}^2$.

The LH changed in a range from -0.4 to 6.1 W/m^2 with a slightly increased mean (0.7 W/m^2). Additionally, as shown in Figure 7b, the three components of LH were increased, and the order from high to low was as follows: ground evaporative heat to atmosphere ($-3.8 \sim 0.47 \sim 10.0 \text{ W/m}^2$), transpiration flux ($-1.2 \sim 0.09 \sim 0.16 \text{ W/m}^2$) and vegetation canopy evaporative heat to atmosphere ($-0.3 \sim 0.07 \sim 1.9 \text{ W/m}^2$).

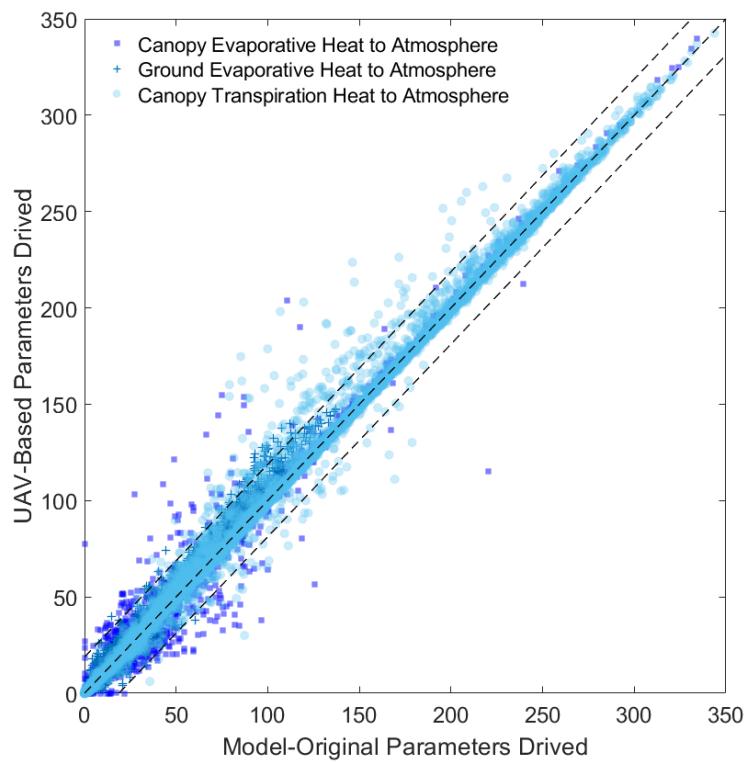
Furthermore, in order to see the more detailed impact, the energy fluxes simulated by the UAV-based canopy parameters and the model's original values were compared in terms of the hourly averages through the diurnal cycle. Figure 8 shows the diurnal variation of SH, LH and G. It can be seen that all three energy components presented significant diurnal variations, and the corresponding curves appeared with a single peak at noon and a value close to zero or negative at night.

On the other hand, Figure 8 also shows the diurnal changes of surface heat fluxes caused by different driving factors. This indicates that the replacement of canopy parameters using UAV-based results mainly has an effect on LH during the day and night, while it influences the SH and G in the opposite direction at night. After replacing canopy parameters with UAV-based results, the simulated LH flux was decreased by up to -11% in the midday while increasing up to 15% in the nighttime. This was probably due to the improvement of canopy characteristics, which directly affected the calculation of canopy stomata [19].

Moreover, while the G increased by about $5\sim 30\%$ at the same time and showed an increasing trend in the daytime, the SH decreased by about $10\sim 60\%$ at nighttime. At the time of the day and night boundary, the SH and the G showed the largest change, which might be due to the breakage of the boundary layer [53]. A high sensitivity of the canopy height to evapotranspiration was also reported in a previous study [54]. Although the changes of surface heat budgets in their study and ours have shown a similarly small range, the description of the canopy characteristics of the land surface model still needs to be improved due to the expression of heterogeneity for the underlying surface being overlooked.



(a) Simulated surface heat fluxes



(b) Simulated latent heat flux subitems

Figure 7. Comparison of surface heat flux items caused by different driving factors.

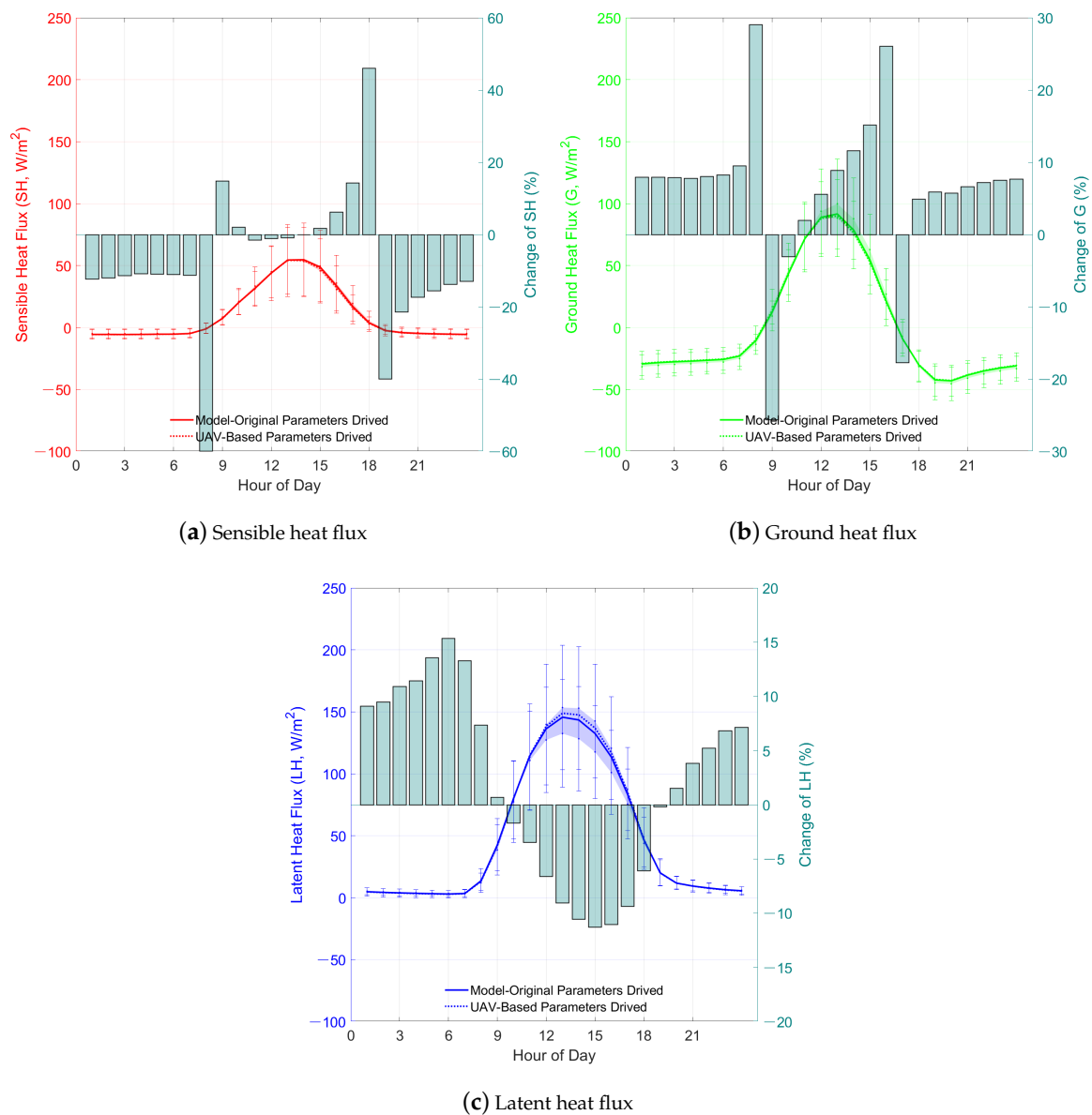


Figure 8. Diurnal changes of surface heat fluxes caused by different driving factors.

4. Discussion

4.1. Issues Related to Canopy Exchange Coefficients

To understand the influence of canopy parameters on the above-mentioned surface energy changes, we extracted the simulated results of the canopy exchange coefficient. As shown in Figure 9a, for the canopy heat exchange coefficient, the parameters driven by UAV measurement increased by about 0.5~2% compared with that of the default model. This would be the main reason for the change of the surface sensible heat simulation.

At the same time, Figure 9b shows the simulation results of the canopy momentum exchange coefficient. It can be seen that, after changing the parameters of canopy height and crown radius, the exchange coefficient of momentum increased by nearly 5% during the daytime. As the momentum exchange coefficient of the canopy was calculated by the aerodynamic resistance for momentum over the canopy, it might have an impact on the variation of wind speed in the canopy. However, because the model cannot deliver the wind profiles inside and outside the canopy, a mesoscale meteorological model should be carried out in the next phase to investigate its effect on turbulence dissipation.

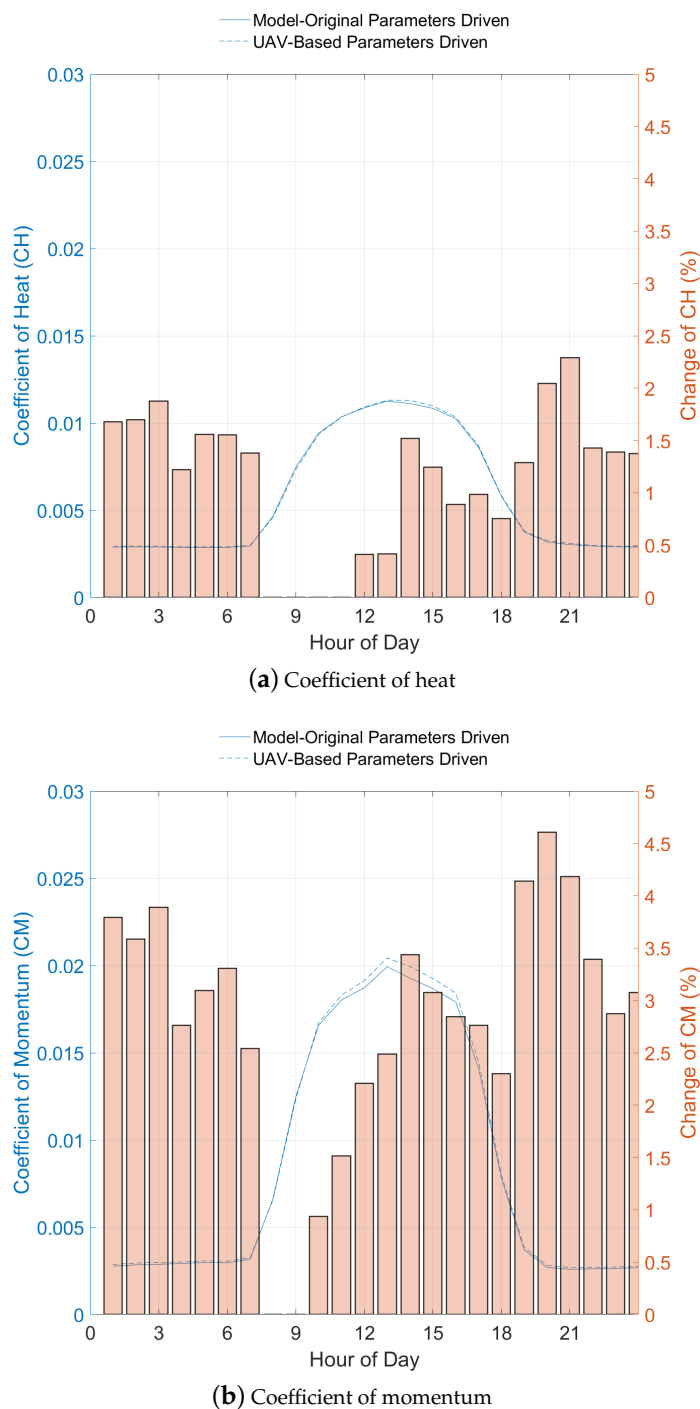
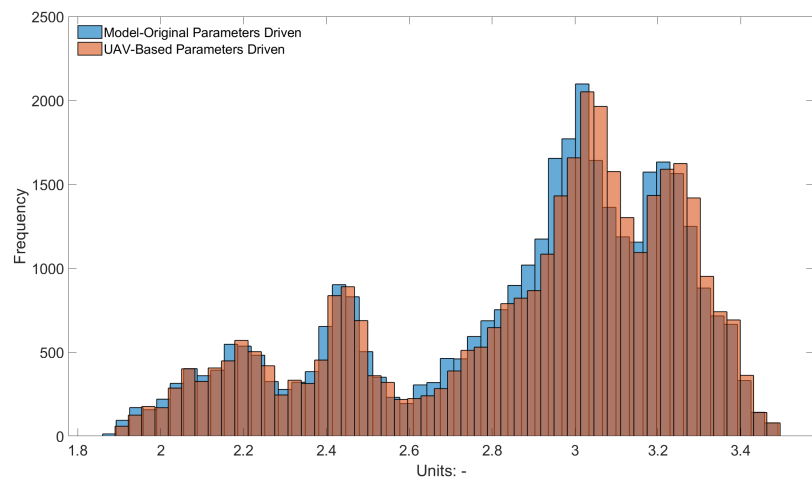


Figure 9. Distribution of simulated canopy exchange coefficients.

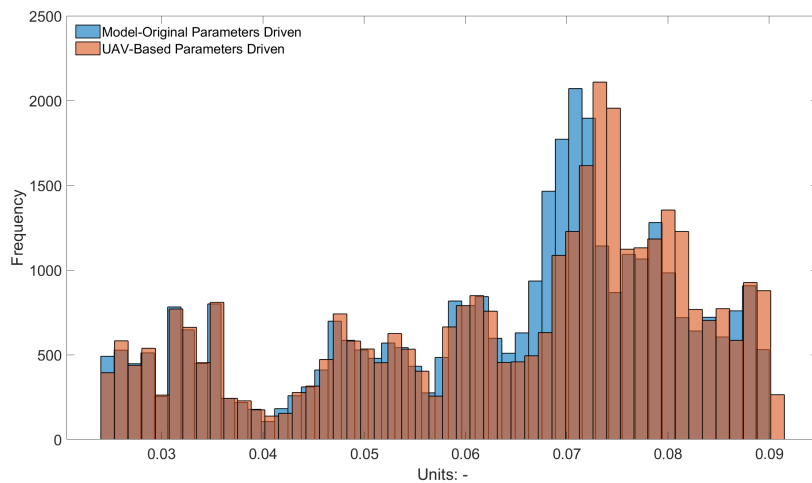
4.2. Issues Related to Vegetation Variables

The Noah-MP land surface model includes a routine calculation for the dynamic simulation of vegetation carbon assimilation processes, while the 3D vegetation model in the radiation transfer scheme uses canopy height to compute the total available energy at the vegetation surface [55]. Figure 10 shows the simulated vegetation variables of the Noah-MP land surface model; this indicates that the input of the UAV’s observed canopy height and radius increased the average leaf area index about 1.58×10^{-2} , the stem area index about 1.1×10^{-3} and the green vegetation fraction about 1.8×10^{-3} during the simulated period. The variation mainly appeared on the right sides of each frequency peak of the above variables, which means that more accurate canopy parameters input can

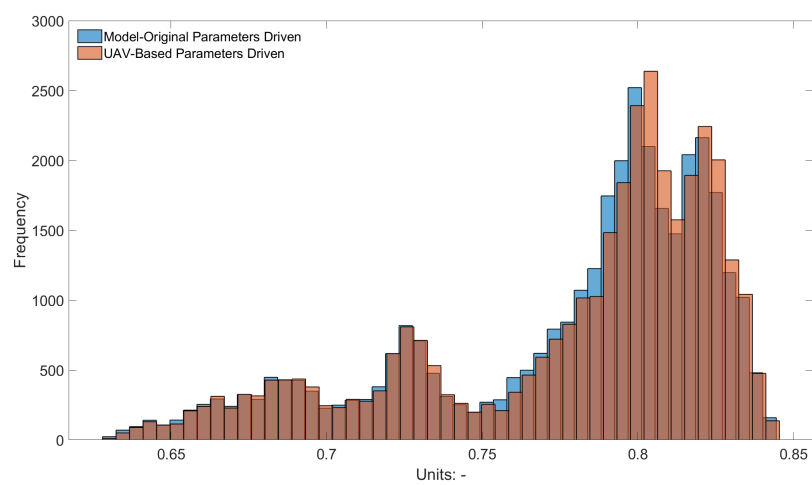
restrict and improve the estimation of vegetation carbon assimilation processes inside the land surface model. These results could influence the temperature and the vegetation growth characteristics [7].



(a) Leaf area index



(b) Stem area index



(c) Green vegetation fraction

Figure 10. Distribution of simulated vegetation features.

5. Conclusions

In this study, a method to obtain local canopy parameters by unmanned aerial vehicle photogrammetry was applied, and then a simulation with the Noah-MP model was performed over a typical subtropical forest area in South China. The results demonstrated that this method could represent the description of forest canopy characteristics in a more detailed manner. The canopy height in the CN-Din area was fitted as a Weibull distribution, while the canopy radius followed a Burr distribution; the medians (standard deviations) of the UAV-based tree height and crown radius were 12.2 ± 5.4 and 1.9 ± 1.5 m, respectively. It is worthwhile to note that this result was still insufficient in comparison with UAV-borne LiDAR systems. Overall, it was found that this method had strong deliverability, reasonable cost and acceptable precision and could obtain the forest land surface parameters of several square kilometers and improve the land surface model.

The updating of these local canopy parameters would significantly affect the simulation of energy fluxes, especially for the latent heat flux, which could decrease up to -11% in the midday while increasing up to 15% in the nighttime. Additionally, the sensible heat flux decreased by about $10\sim 60\%$ at nighttime, while the ground heat flux increased by about $5\sim 30\%$ at the same time, showing an increasing trend during the daytime. Furthermore, the updating of local canopy parameters could also change the canopy heat exchange coefficient through the slight increase of vegetation variables.

Although the changes of surface heat budgets showed a small range, the description of the canopy characteristics of the land surface model still needs to be improved. Moreover, the updating of canopy parameters could increase the exchange coefficient of momentum by nearly 5% during the daytime. Finally, the calculation of the total available energy at the vegetation surface showed that the input of the UAV observed canopy height and radius could increase the average leaf area index by about 1.58×10^{-2} , the stem area index by about 1.1×10^{-3} and the green vegetation fraction by about 1.8×10^{-3} during the simulated period.

To further enhance the capability of simulating the surface heat budgets of land surface models and to improve the land surface parameterization scheme of climate and meteorological models, a work combining both UAV LiDAR and photogrammetry should be considered, as LiDAR can provide a more accurate 3D canopy structure, which influences the surface wind profile and the momentum.

Author Contributions: Conceptualization, M.C.; formal analysis, J.C., B.C. and Q.Z.; methodology, M.C. and S.Z.; software, S.Z.; supervision, X.W.; validation, J.C., B.C. and Q.Z.; visualization, S.Z.; writing—original draft, M.C.; writing—review and editing, W.C., S.J. and P.K. All authors have read and agreed to the published version of the manuscript.

Funding: This research was funded by the National Key Research and Development Plan, grant number 2017YFC0210103, National Natural Science Foundation, grant number 41705123, Special Fund Project for Science and Technology Innovation Strategy of Guangdong Province, grant number 2019B121205004, Funding from the Research Center on Low-carbon Economy for Guangzhou Region, grant number 20JNZS46, and the Environmental Scientific Research Project in Shenzhen, grant number GXZX-19042SZGK.

Acknowledgments: This work was supported by the Dinghushan Forest Ecosystem Research Station, Chinese Academy of Sciences and the High-Performance Public Computing Service Platform of Jinan University.

Conflicts of Interest: The authors declare no conflict of interest.

References

1. Pitman, A. The evolution of, and revolution in, land surface schemes designed for climate models. *Int. J. Climatol.* **2003**, *23*, 479–510. [[CrossRef](#)]
2. Zhao, W.; Li, A. A review on land surface processes modelling over complex terrain. *Adv. Meteorol.* **2015**, *2015*, 607181. [[CrossRef](#)]
3. Chen, F.; Kusaka, H.; Bornstein, R.; Ching, J.; Grimmond, C.; Grossman-Clarke, S.; Loridan, T.; Manning, K.W.; Martilli, A.; Miao, S.; et al. The integrated WRF/urban modelling system: Development, evaluation, and applications to urban environmental problems. *Int. J. Climatol.* **2011**, *31*, 273–288. [[CrossRef](#)]
4. Fang, H.; Baret, F.; Plummer, S.; Schaepman-Strub, G. An overview of global leaf area index (LAI): Methods, products, validation, and applications. *Rev. Geophys.* **2019**, *57*, 739–799. [[CrossRef](#)]

5. Chang, M.; Fan, S.; Wang, X. Impact of refined land-cover data on WRF performance over the Pearl River Delta region, China. *Huanjing Kexue Xuebao/Acta Sci. Circumstantiae* **2014**, *34*. [[CrossRef](#)]
6. Eagleson, P.S. *Land Surface Processes in Atmospheric General Circulation Models*; Cambridge University Press: Cambridge, UK, 2011.
7. Liu, X.; Chen, F.; Barlage, M.; Zhou, G.; Niyogi, D. Noah-MP-Crop: Introducing dynamic crop growth in the Noah-MP land surface model. *J. Geophys. Res. Atmos.* **2016**, *121*, 13–953. [[CrossRef](#)]
8. Yin, G.; Li, J.; Liu, Q.; Fan, W.; Xu, B.; Zeng, Y.; Zhao, J. Regional leaf area index retrieval based on remote sensing: The role of radiative transfer model selection. *Remote Sens.* **2015**, *7*, 4604–4625. [[CrossRef](#)]
9. Xue, Y.; Sellers, P.; Kinter, J.; Shukla, J. A simplified biosphere model for global climate studies. *J. Clim.* **1991**, *4*, 345–364. [[CrossRef](#)]
10. Chen, F.; Dudhia, J. Coupling an advanced land surface–hydrology model with the Penn State–NCAR MM5 modeling system. Part I: Model implementation and sensitivity. *Mon. Weather Rev.* **2001**, *129*, 569–585. [[CrossRef](#)]
11. Xiu, A.; Pleim, J.E. Development of a land surface model. Part I: Application in a mesoscale meteorological model. *J. Appl. Meteorol.* **2001**, *40*, 192–209. [[CrossRef](#)]
12. Mitchell, K. *The Community Noah Land-Surface Model (LSM) User's Guide. Public Release Version 2.7.1*; National Weather Service, National Center for Environmental Prediction: Camp Springs, MD, USA, 2005.
13. Niu, G.Y.; Yang, Z.L.; Mitchell, K.E.; Chen, F.; Ek, M.B.; Barlage, M.; Kumar, A.; Manning, K.; Niyogi, D.; Rosero, E.; et al. The community Noah land surface model with multiparameterization options (Noah-MP): 1. Model description and evaluation with local-scale measurements. *J. Geophys. Res. D Atmos.* **2011**, *116*. [[CrossRef](#)]
14. Ke, Y.; Leung, L.; Huang, M.; Coleman, A.M.; Li, H.; Wigmosta, M.S. Development of high resolution land surface parameters for the Community Land Model. *Geosci. Model Dev.* **2012**, *5*, 1341. [[CrossRef](#)]
15. Smirnova, T.G.; Brown, J.M.; Benjamin, S.G.; Kenyon, J.S. Modifications to the rapid update cycle land surface model (RUC LSM) available in the weather research and forecasting (WRF) model. *Mon. Weather Rev.* **2016**, *144*, 1851–1865. [[CrossRef](#)]
16. Baldocchi, D.D.; Hicks, B.B.; Camara, P. A canopy stomatal resistance model for gaseous deposition to vegetated surfaces. *Atmos. Environ. (1967)* **1987**, *21*, 91–101. [[CrossRef](#)]
17. Droppo, J.G. *Improved Formulations for Air-Surface Exchanges Related to National Security Needs: Dry Deposition Models*; Pacific Northwest National Lab. (PNNL): Richland, WA, USA, 2006.
18. Huang, D.; Knyazikhin, Y.; Wang, W.; Deering, D.W.; Stenberg, P.; Shabanov, N.; Tan, B.; Myneni, R.B. Stochastic transport theory for investigating the three-dimensional canopy structure from space measurements. *Remote Sens. Environ.* **2008**, *112*, 35–50. [[CrossRef](#)]
19. Ma, Y.; Liu, H. An advanced multiple-layer canopy model in the WRF model with large-eddy simulations to simulate canopy flows and scalar transport under different stability conditions. *J. Adv. Model. Earth Syst.* **2019**, *11*, 2330–2351. [[CrossRef](#)]
20. Gan, Y.; Liang, X.Z.; Duan, Q.; Chen, F.; Li, J.; Zhang, Y. Assessment and reduction of the physical parameterization uncertainty for Noah-MP Land Surface Model. *Water Resour. Res.* **2019**, *55*, 5518–5538. [[CrossRef](#)]
21. Haynes, K.; Baker, I.; Denning, S. *Simple Biosphere Model Version 4.2 (SiB4) Technical Description*; Colorado State University: Fort Collins, CO, USA, 2020.
22. Weiss, M.; Baret, F. Using 3D point clouds derived from UAV RGB imagery to describe vineyard 3D macro-structure. *Remote Sens.* **2017**, *9*, 111. [[CrossRef](#)]
23. Guo, Q.; Su, Y.; Hu, T.; Zhao, X.; Wu, F.; Li, Y.; Liu, J.; Chen, L.; Xu, G.; Lin, G.; et al. An integrated UAV-borne lidar system for 3D habitat mapping in three forest ecosystems across China. *Int. J. Remote. Sens.* **2017**, *38*, 2954–2972. [[CrossRef](#)]
24. Liu, K.; Shen, X.; Cao, L.; Wang, G.; Cao, F. Estimating forest structural attributes using UAV-LiDAR data in Ginkgo plantations. *ISPRS J. Photogramm. Remote Sens.* **2018**, *146*, 465–482. [[CrossRef](#)]
25. McNeil, B.E.; Pisek, J.; Lepisk, H.; Flamenco, E.A. Measuring leaf angle distribution in broadleaf canopies using UAVs. *Agric. For. Meteorol.* **2016**, *218*, 204–208. [[CrossRef](#)]
26. Jiménez López, J.; Mulero-Pázmány, M. Drones for conservation in protected areas: Present and future. *Drones* **2019**, *3*, 10. [[CrossRef](#)]

27. Chung, C.H.; Huang, C.Y. Hindcasting tree heights in tropical forests using time-series unmanned aerial vehicle imagery. *Agric. For. Meteorol.* **2020**, *290*, 108029. [[CrossRef](#)]
28. Brüllhardt, M.; Rotach, P.; Schleppi, P.; Bugmann, H. Vertical light transmission profiles in structured mixed deciduous forest canopies assessed by UAV-based hemispherical photography and photogrammetric vegetation height models. *Agric. For. Meteorol.* **2020**, *281*, 107843. [[CrossRef](#)]
29. Wallace, L.; Lucieer, A.; Watson, C.; Turner, D. Development of a UAV-LiDAR system with application to forest inventory. *Remote Sens.* **2012**, *4*, 1519–1543. [[CrossRef](#)]
30. Guimarães, N.; Pádua, L.; Marques, P.; Silva, N.; Peres, E.; Sousa, J.J. Forestry Remote Sensing from Unmanned Aerial Vehicles: A Review Focusing on the Data, Processing and Potentialities. *Remote Sens.* **2020**, *12*, 1046. [[CrossRef](#)]
31. Xu, Z.; Shen, X.; Cao, L.; Coops, N.C.; Goodbody, T.R.; Zhong, T.; Zhao, W.; Sun, Q.; Ba, S.; Zhang, Z.; et al. Tree species classification using UAS-based digital aerial photogrammetry point clouds and multispectral imageries in subtropical natural forests. *Int. J. Appl. Earth Obs. Geoinf.* **2020**, *92*, 102173. [[CrossRef](#)]
32. Chang, M.; Liao, W.; Wang, X.; Zhang, Q.; Chen, W.; Wu, Z.; Hu, Z. An optimal ensemble of the Noah-MP land surface model for simulating surface heat fluxes over a typical subtropical forest in South China. *Agric. For. Meteorol.* **2020**, *281*, 107815. [[CrossRef](#)]
33. Yan, J.H.; Zhou, G.Y.; Zhang, D.Q.; Tang, X.L.; Wang, X. Different patterns of changes in the dry season diameter at breast height of dominant and evergreen tree species in a mature subtropical forest in South China. *J. Integr. Plant Biol.* **2006**, *48*, 906–913. [[CrossRef](#)]
34. Zhou, G.; Guan, L.; Wei, X.; Zhang, D.; Zhang, Q.; Yan, J.; Wen, D.; Liu, J.; Liu, S.; Huang, Z.; et al. Litterfall production along successional and altitudinal gradients of subtropical monsoon evergreen broadleaved forests in Guangdong, China. *Plant Ecol.* **2007**, *188*, 77–89. [[CrossRef](#)]
35. Yu, X.; Pan, Y.; Song, W.; Li, S.; Li, D.; Zhu, M.; Zhou, H.; Zhang, Y.; Li, D.; Yu, J.; et al. Wet and Dry Nitrogen Depositions in the Pearl River Delta, South China: Observations at Three Typical Sites with an Emphasis on Water-Soluble Organic Nitrogen. *J. Geophys. Res. Atmos.* **2020**, *125*, e2019JD030983. [[CrossRef](#)]
36. Puliti, S.; Talbot, B.; Astrup, R. Tree-stump detection, segmentation, classification, and measurement using unmanned aerial vehicle (UAV) imagery. *Forests* **2018**, *9*, 102. [[CrossRef](#)]
37. Larrinaga, A.R.; Brotons, L. Greenness Indices from a Low-Cost UAV Imagery as Tools for Monitoring Post-Fire Forest Recovery. *Drones* **2019**, *3*, 6. [[CrossRef](#)]
38. Pix4D SA. *Pix4Dmapper 4.1 User Manual*; Pix4D SA: Lausanne, Switzerland, 2017.
39. Brunzell, N.A.; de Oliveira, G.; Barlage, M.; Shimabukuro, Y.; Moraes, E.; Aragão, L. Examination of seasonal water and carbon dynamics in eastern Amazonia: A comparison of Noah-MP and MODIS. *Theor. Appl. Climatol.* **2020**, 1–16. [[CrossRef](#)]
40. Ma, Q.; Su, Y.; Guo, Q. Comparison of canopy cover estimations from airborne LiDAR, aerial imagery, and satellite imagery. *IEEE J. Sel. Top. Appl. Earth Obs. Remote Sens.* **2017**, *10*, 4225–4236. [[CrossRef](#)]
41. Hu, T.; Ma, Q.; Su, Y.; Battles, J.J.; Collins, B.M.; Stephens, S.L.; Kelly, M.; Guo, Q. A simple and integrated approach for fire severity assessment using bi-temporal airborne LiDAR data. *Int. J. Appl. Earth Obs. Geoinf.* **2019**, *78*, 25–38. [[CrossRef](#)]
42. Zhang, Q.; Chang, M.; Zhou, S.; Chen, W.; Wang, X.; Liao, W.; Dai, J.; Wu, Z. Evaluate dry deposition velocity of the nitrogen oxides using Noah-MP physics ensemble simulations for the Dinghushan Forest, Southern China. *Asia-Pac. J. Atmos. Sci.* **2017**, *53*, 519–536. [[CrossRef](#)]
43. Dickinson, R.E.; Shaikh, M.; Bryant, R.; Graulich, L. Interactive canopies for a climate model. *J. Clim.* **1998**, *11*, 2823–2836. [[CrossRef](#)]
44. Ball, J.T.; Woodrow, I.E.; Berry, J.A. A model predicting stomatal conductance and its contribution to the control of photosynthesis under different environmental conditions. In *Progress in Photosynthesis Research*; Springer: Dordrecht, The Netherlands, 1987; pp. 221–224.
45. Chen, F.; Mitchell, K.; Schaake, J.; Xue, Y.; Pan, H.L.; Koren, V.; Duan, Q.Y.; Ek, M.; Betts, A. Modeling of land surface evaporation by four schemes and comparison with FIFE observations. *J. Geophys. Res. D Atmos.* **1996**, *101*, 7251–7268. [[CrossRef](#)]
46. Niu, G.Y.; Yang, Z.L.; Dickinson, R.E.; Gulden, L.E.; Su, H. Development of a simple groundwater model for use in climate models and evaluation with Gravity Recovery and Climate Experiment data. *J. Geophys. Res. D Atmos.* **2007**, *112*. [[CrossRef](#)]

47. Chen, F.; Janjić, Z.; Mitchell, K. Impact of atmospheric surface-layer parameterizations in the new land-surface scheme of the NCEP mesoscale Eta model. *Bound.-Layer Meteorol.* **1997**, *85*, 391–421. [[CrossRef](#)]
48. Niu, G.Y.; Yang, Z.L. Effects of vegetation canopy processes on snow surface energy and mass balances. *J. Geophys. Res. D Atmos.* **2004**, *109*. [[CrossRef](#)]
49. Niu, G.Y.; Yang, Z.L. Effects of frozen soil on snowmelt runoff and soil water storage at a continental scale. *J. Hydrometeorol.* **2006**, *7*, 937–952. [[CrossRef](#)]
50. Verseghy, D.L. CLASS—A Canadian land surface scheme for GCMs. I. Soil model. *Int. J. Climatol.* **1991**, *11*, 111–133. [[CrossRef](#)]
51. Jordan, R. *A One-Dimensional Temperature Model for a Snow Cover: Technical Documentation for Sntherm*. 89; Technical Report; Cold Regions Research and Engineering Lab.: Hanover, NH, USA, 1991.
52. Barlage, M.; Tewari, M.; Chen, F.; Miguez-Macho, G.; Yang, Z.L.; Niu, G.Y. The effect of groundwater interaction in North American regional climate simulations with WRF/Noah-MP. *Clim. Chang.* **2015**, *129*, 485–498. [[CrossRef](#)]
53. Serafin, S.; Adler, B.; Cuxart, J.; De Wekker, S.F.; Gohm, A.; Grisogono, B.; Kalthoff, N.; Kirshbaum, D.J.; Rotach, M.W.; Schmidli, J.; et al. Exchange processes in the atmospheric boundary layer over mountainous terrain. *Atmosphere* **2018**, *9*, 102. [[CrossRef](#)]
54. Cuntz, M.; Mai, J.; Zink, M.; Thober, S.; Kumar, R.; Schäfer, D.; Schrön, M.; Craven, J.; Rakovec, O.; Spieler, D.; et al. Computationally inexpensive identification of noninformative model parameters by sequential screening. *Water Resour. Res.* **2015**, *51*, 6417–6441. [[CrossRef](#)]
55. Arsenault, K.R.; Nearing, G.S.; Wang, S.; Yatheendradas, S.; Peters-Lidard, C.D. Parameter sensitivity of the noah-mp land surface model with dynamic vegetation. *J. Hydrometeorol.* **2018**, *19*, 815–830. [[CrossRef](#)]

Publisher’s Note: MDPI stays neutral with regard to jurisdictional claims in published maps and institutional affiliations.



© 2020 by the authors. Licensee MDPI, Basel, Switzerland. This article is an open access article distributed under the terms and conditions of the Creative Commons Attribution (CC BY) license (<http://creativecommons.org/licenses/by/4.0/>).